Twinning and rotational deformation of nanocrystalline NiTi under shock loading

C. Lv,[1] X. P. Zhang,[1] G. J. Wang,[1,*] F. Zhao,[2] N. Luo,[3] S. N. Bland,[4] F. L. Tan,[1] J. H. Zhao,[5] C. L. Liu,[6] and C. W. Sun[1]

[1]*Institute of Fluid Physics, China Academy of Engineering Physics, Mianyang 621999, China*

[2]*Institute of Material Structure and Strength, Chengdu University, Chengdu 610106, China*

[3]*State Key Laboratory for Geomechanics and Deep Underground Engineering, School of Mechanics and Civil Engineering, China University of Mining and Technology, Xuzhou 221116, China*

[4]*Imperial College London, Blackett Laboratory, London SW7 2AZ, United Kingdom*

[5]*Institute of applied Electronics, China Academy of Engineering Physics, Mianyang 621999, China*

[6]*China Academy of Engineering Physics, Mianyang 621999, China*

(Received 6 May 2020; revised 24 July 2020; accepted 8 September 2020; published 25 September 2020)

Understanding the formation of twins and new grains (NGs) in B2 austenite NiTi alloys under shock loading is of significance and importance for its science insights and engineering applications. However, the formation of {112} twin in austenite phase under shock loading is still controversial, and the NGs' evolution under shock loading is unclear. The Electron Backscatter Diffraction characterizations and x-ray diffraction analyses of the NiTi samples recovered from the shock experiments reveal that the main deformation modes include dislocations, twins, and new grains, etc. Similar phenomena are also obtained in our nonequilibrium molecular dynamics simulations for nanocrystalline NiTi (nc-NiTi) with limited-duration-pulse shock loading. Simulations confirmed that {112} twins in austenite phase can be formed by successively gliding a displacement of $\frac{a}{3}[111]$ on $(\bar{2}11)$ plane. It can occur in both shock compression and release stages, in addition, the grain boundaries triple junction and the interaction of slip bands with different slip systems can serve as the nucleation of twins. Moreover, that the nanoscale rotational deformation leads to the formation of NGs is found in our simulation of nc-NiTi, without experiencing the conventional disorder-recrystallization-grain refinement stages in the corresponding region. Related to shear stress τ, the shock loading velocity U_p plays the key role in the formations of twins and NGs. These early successes may hope to get some insights into the deformation mechanism of NiTi under shock loading.

DOI: 10.1103/PhysRevMaterials.4.093607

I. INTRODUCTION

Due to its excellent mechanical properties, corrosion resistance, and biocompatibility [1–4], NiTi alloys are extensively used in aviation components, engineering machinery, and biomedicine. Lots of research had been performed to better understand the properties of NiTi and further its applications [1–6,25,26]. In recent years there have been growing interests in extreme cases, including jet turbine blades, seismic test equipment, and shock mitigating structures [5–7]; hence exploring its physical and mechanical properties under shock loading is important. Generally, two main experimental methods are used to study the dynamic behavior of NiTi alloys under shock loading: one-dimensional (1D) stress loading, as produced by a Split-Hopkinson pressure bar (SHPB) [8–12]; and one-dimensional strain loading, such as that produced by a gas gun, or in laser-driven experiments [13,14,26]. Utilizing these techniques, researchers have explored the macroscopic behavior of NiTi alloys, studied their equation of state (EOS), stress-strain relationships, spall strengths, damage evolution, etc. However, only few studies have focused on the deformation and microstructure characteristics of NiTi under shock loading. Furthermore, most of these studies were devoted to revealing the phenomena related to phase transformation between austenite and martensite phase of NiTi [15], and less attention has been paid to dislocations, twinning, and new grain, which controls its plastic deformation.

There have already been several molecular dynamics (MD) studies of NiTi alloys. Yin *et al.* adopted the improved embedded-atom method (EAM) potential function of Zhong [16] to simulate the shock behaviors of finite-size single crystalline NiTi at different initial ambient temperatures, observing the shock deformation modes change from phase transformation and twinning to simple dislocation motion as the initial ambient temperature increased [17]. Yazdandoost *et al.* further studied the relationship between shock behaviors and the energy dissipation under the local impact loading of single crystalline and polycrystalline NiTi, with phase transformation and plastic deformation detected by a criterion based on equivalent shear strains, and the influence of grain size and grain boundary (GB) type were considered [18]. Wang *et al.* used the second-nearest-neighbor modified embedded-atom method (2NN MEAM) potential function newly developed by Ko *et al.* [19] to study the phase transformation and twinning of single crystalline NiTi under one-dimensional plate shock loading, showing martensitic transformations and reverse martensitic transformations were related with twinning and detwinning, respectively [20].

*wangguiji@126.com

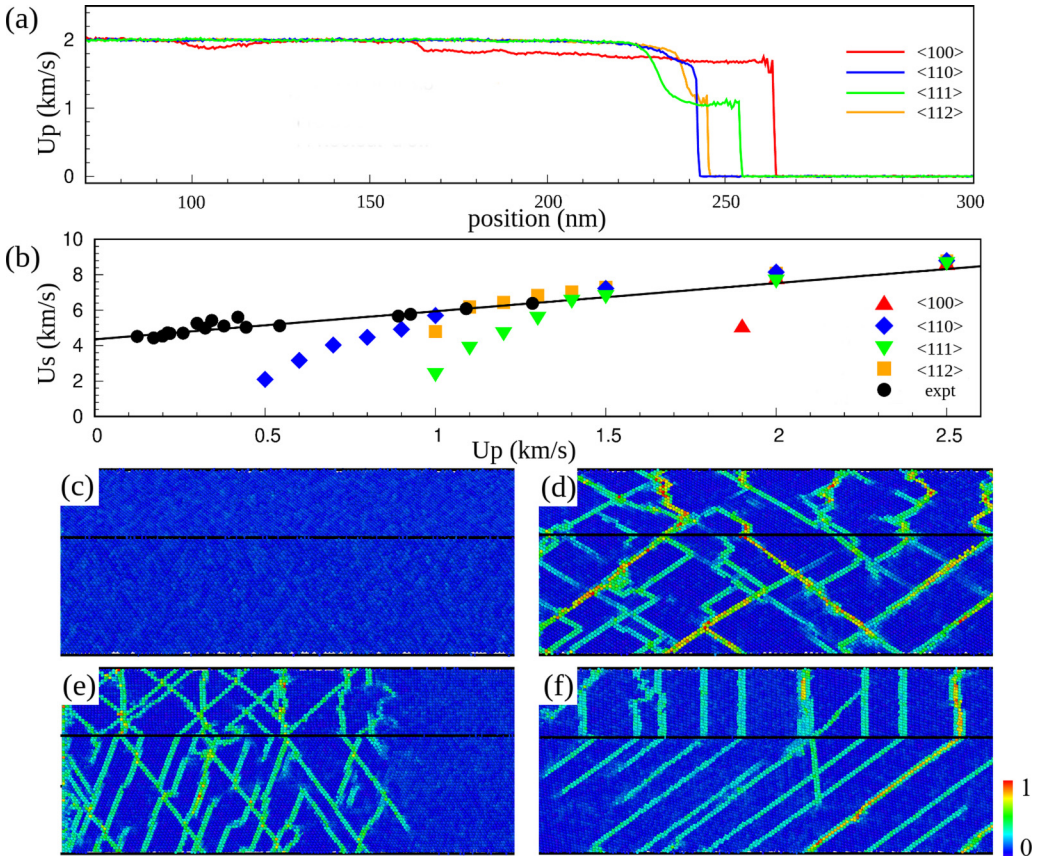

FIG. 1. (a) Particle velocity profile *Up* for shock loading along ⟨100⟩, ⟨110⟩, ⟨111⟩ and ⟨112⟩, respectively, at $t = 15.0$ ps. (b) The shock wave velocity-particle velocity (*Us–Up*) plots obtained from our NEMD simulations of single crystalline and polycrystalline NiTi experiments [21–26]. The line represents the linear fitting to the experimental results: $\mathrm{Us} = 4.351 + 1.588\,\mathrm{U_p}$ [26]. Only the plastic wave velocities are plotted in Fig. 1(b) for clarity. (c)–(f) Shock-induced deformation in single crystalline NiTi along the ⟨100⟩, ⟨110⟩, ⟨111⟩ and ⟨112⟩ direction, respectively. Characterization by von Mises shear stain analysis.

Contrary to above simulations, however, our previous shock loading experiments have seen no evidence of phase transformation from B2 austenite structures in the velocimetry data and deduced Lagrangian sound speeds [26]. In an ideal world, we would conduct real-time diagnosis of microstructural evolution process of shocked samples using advanced x-ray light sources including third-generation synchrotrons and x-ray free-electron lasers [27]. Even so, these techniques are only now becoming viable, and beam time can be both expensive and difficult to obtain, especially for new users. Metallographic analyses of shock recovered samples, e.g., electron backscatter diffraction (EBSD), meanwhile, is a well proven tool. It can be used to identify the microstructure of the recovered samples, and to better collate MD simulations. MD simulations could bridge the mesoscale characteristics and microstructure. It can give a certain microscopic explanation for many phenomena that are difficult to understand in theoretical analysis and observe in experiments, then we can further understand the physical phenomena and essence.

In summary the goal of this paper is to discover and obtain new insights into microscale dynamics of polycrystalline NiTi under shock loading via metallographic analysis of shock recovered samples and detailed molecular dynamics (MD) simulations. The simulation methods and experiments techniques are described in Sec. II, and results and discussion in Sec. III, followed by the conclusions in Sec. IV.

II. SIMULATION METHODS AND EXPERIMENTAL TECHNIQUES

A. Details of models and simulations

The nonequilibrium molecular dynamics simulations (NEMD) are carried out by using the large-scale atomic molecular massively parallel simulators (LAMMPS) code [28]. We adopt an embedded atom method (EAM) potential, which was developed by Lai *et al.* [29] and then improved by Zhong *et al.* [16]. This potential well describes the relationship between mechanical properties and microstructures of NiTi under static compression/tension. It also has a reasonable explanation for NiTi phase transformation caused by temperature changes.

To verify and validate the applicability and reliability of the potential function under shock loading with high strain rates, we carry out NEMD simulations of single crystalline NiTi (sc-NiTi) to fit the shock wave velocity-particle velocity (U_s-U_p) relation [Fig. 1(b)]. Its specific contents include calculating the 1D shock propagation profiles of certain loading direction sc-NiTi under different shock loading velocities U_p and different loading directions [Fig. 1(a)]. The U_p ranging from

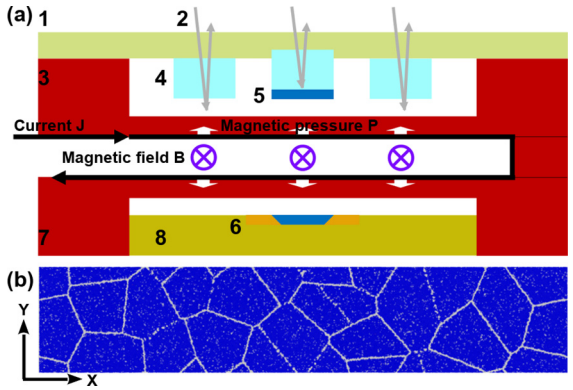

FIG. 2. (a) Schematic of magnetically driven shock compression experiment and sample recovery. 1: PMMA holders; 2: DLHV pins; 3: Anode panel; 4: Windows; 5: Sample; 6: Momentum trapping rings; 7: Cathode panel; 8: Copper momentum trapping. (b) Columnar nc-NiTi model characteristic by CNA methods: the blue region represents B2 austenite NiTi, the white region represents GBs or atoms in disorder.

0.5–2.5 km s^{-1}. And the loading directions of sc-NiTi along the x axis are ⟨100⟩, ⟨110⟩, ⟨111⟩, and ⟨112⟩, respectively. The shock experimental data for polycrystalline NiTi are also used for comparison [21–26]. In addition, our previous experimental work has given the Hugoniot relation $U_s = 4.351 + 1.588U_p$ for 0.1 km s^{-1} $< U_p <$ 1.4 km s^{-1} [26]. Although there is no clear relationship to build polycrystalline Hugoniot from single crystalline Hugoniot, our sc-NiTi NEMD simulations show reasonable agreement with the polycrystalline experimental results, especially at high shock loading velocities [30]. It should be noted that the deviation at relatively low U_p is a common phenomenon in shock loading NEMD simulation for sc-NiTi [31].

Figures 1(c)–1(f) show snapshots for different shock loading direction at $t = 10.0$ ps ($U_p = 1.0$ km s^{-1}). The calculated results exhibit obvious anisotropy in elasticity and plasticity for diverse loading direction. For the (110), (111), and (112) shock, the elastic-plastic phenomena appears obviously. While for the (100) shock, only elastic wave occurs. We adopt the von Mises shear strain (η_i^{Mises}) analysis [32] to sc-NiTi model after shock wave passing through. The $\eta_i^{\text{Mises}} = 0$ indicates that only elastic deformation, η_i^{Mises} could increase with the rise of plastic deformation, this means that η_i^{Mises} can be used to identify dislocations, twins, etc. For example, the η_i^{Mises} for (100) loading is around zero and it remains elastic until 1.8 km s^{-1}.

The Voronoi tessellation method is used to construct a columnar nanocrystalline NiTi (nc-NiTi) model [33] [Fig. 2(b)]. Each grain is oriented with $[0\bar{1}1]$ direction along z axis, but with various rotations in the x-y plane. Referring to our previous experimental work [26], we adopt the B2 NiTi austenite structure in the initial model. The lattice constant of the unit cell in the B2 austenite phase is 3.008 Å [16], and the average grain diameter is about 20 nm. The dimensions of the configuration after the Voronoi tessellation division are about 200 nm × 40 nm × 1.2 nm, then we replicate the model along the x axis (shock direction) three times to produce larger systems for shock simulations. Finally nanocrystalline $Ni_{52}Ti_{48}$ model is obtained by randomly replacing some Ti atoms by Ni atoms in the nanocrystalline $Ni_{50}Ti_{50}$.

Of all the simulations in this study, immediately before shock loading, the columnar nanocrystalline $Ni_{52}Ti_{48}$ models were relaxed for 20.0 ps in a constrained temperature and pressure (NPT) integrator [34,35] to eliminate residual stress and obtain GB conditions close to real state. To simulate one-dimensional strain loading, periodic boundary conditions are applied along the y-axis and z-axis directions, and free boundary conditions are applied along the x axis (shock direction). A time step of 0.5 ps is used throughout the simulations, and a microcanonical (NVE) ensemble is utilized [36]. Note that the stress unloading (release) is often ignored by MD simulations, but it exactly exists in experiments [37]. In this study, a piston shock method generating shock waves is utilized for simulation, where the piston moves at a constant speed for 35.0 ps, and then it is withdrawn to enable the stress release along loading direction.

B. Molecular simulation analysis methodology

Data visualization and microstructure analysis are based on the common neighbor analysis (CNA) and von Mises stain methods of the OVITO software [38,39]. The CNA method could characterize the local state around the atoms and it has been proven to effectively distinguish between B2 austenite and B19′ martensite phases [40]. The von Mises shear strain η_i^{Mises} describes the atom deformation tensors for better resolution of deformation and structure [32,41]. X-ray diffraction (XRD) intensity is also calculated to confirm that the phase transformation does not occur in our NEMD simulation [42]. The radial distribution function (RDF) measures the probability of finding atoms as a function of distance $\boldsymbol{r}$ from an a particle position $\boldsymbol{r} = 0$ [43]. In addition, changes in crystal orientation, such as twins, new grains, etc., can be resolved by orientation mapping (OM) analysis [44,45].

To better identify the dislocation evolution, the maximum relative displacement (MRD) based on the slip vector method is applied [46–48]. The term slip vector is not the Burgers vector in material science, the definition is as follows:

$$\boldsymbol{S_i} = -\frac{1}{n_s}\sum_{i\neq j}^{N}(\boldsymbol{x_{ij}} - \boldsymbol{X_{ij}}). \tag{1}$$

n is the number of the nearest neighbors to atom i, n_s is the number of the slipped neighbors j, x_{ij}, and X_{ij} represent the vector difference in position (between atoms i and j) in current and reference configurations, respectively [46]. The reference configuration is the initial simulation model without stress or strain. The MRD is defined as the above slip vector with the maximum amplitude instead of the average of sliding vector sum, the definition is as follows [47,48]:

$$\boldsymbol{S_i} = \boldsymbol{x_{ij}} - \boldsymbol{X_{ij}} : |\boldsymbol{x_{ij}} - \boldsymbol{X_{ij}}|_{\max}, \tag{2}$$

the modulus of $\boldsymbol{S_i}$ is $|\boldsymbol{S_i}|$,

For each trajectory file generated by MD simulations, we divided the entire simulation cell into uniform unit along the x axis (1D binning analysis) or both the x and y axes (2D binning analysis) [49,50]. Side length of binning cell is 0.5 nm. Physical properties such as von Mises shear stress τ

were calculated [32], defined as:

$$\tau = \sqrt{3J_2}, \tag{3}$$

where

$$J_2 = \tfrac{1}{6}\{(\sigma_{xx}-\sigma_{yy})^2 + (\sigma_{yy}-\sigma_{zz})^2 + (\sigma_{zz}-\sigma_{xx})^2\} + \sigma_{xy}^2 + \sigma_{yz}^2 + \sigma_{zx,}^2 \tag{4}$$

σ_{xx}, σ_{yy}, σ_{zz}, σ_{xy}, σ_{yz} and σ_{xz} are the stress tensor.

C. Materials and experiment techniques

The polycrystalline $Ni_{52}Ti_{48}$ alloys used in this study come from Chinese Northwestern SMA Incorporation. Samples have a density $\rho_0 = 6.42$ g cm^{-3}, longitudinal sound speed $C_L = 5.434$ km s^{-1}, shear sound speed $C_S = 1.775$ km s^{-1}, bulk sound speed $C_B = 5.032$ km s^{-1} and Poisson's ratio $\nu = 0.436$ at room temperature. The starting and finishing phase transformation temperatures for the martensite and austenite phase are $M_s = -14.6$ °C, $M_f = -19.7$ °C, $A_s = -11.4$ °C, $A_f = -0.7$ °C, respectively, which are obtained by differential scanning calorimetry (DSC). The x-ray diffraction (XRD) results show no martensite phase in the samples as received, and NiTi alloys are in B2 austenite structure at room temperature.

The one-dimensional strain shock experiments are conducted on pulsed power generator CQ-4, which can produce peak current 3 ∼ 4 MA with rising time of 400–600 ns and accelerate the ∼cm flyer plates to velocity 10 ∼ 13 km s^{-1} without being melted [51,52]. The schematic configuration for the shock experiment is shown in Fig. 2(a). The anode and cathode panels of the device are composed of flat aluminum plates, which are symmetrically distributed up and down. The pulsed current J produced by CQ-4 flows through the surfaces of anode and cathode panels as depicted in Fig. 2(a), and then the Lorentz force σ, that is the loading magnetic pressure P, is generated from the interaction between current J and its self-induction magnetic field B. By this force, the prefabricated copper flyer plates are launched and accelerated to high velocity to shock NiTi samples. In experiments, the NiTi samples together with LiF and sapphire windows are glued on a polymethyl methacrylate (PMMA) holder, which is fixed on the anode panel. Dual laser heterodyne velocimetry (DLHV) pins based on the windows are used to record the shock arrival times and interface particle velocities between NiTi sample and sapphire window. The sample recoveries are achieved by impedance matching momentum trapping, which captures the momentum and attenuates the loading stress waves for complete recovery of NiTi samples, we use momentum trapping ring tightly couple copper momentum traps and samples to mitigate lateral rarefaction waves [53]. The microstructures of initially received and shock recovered NiTi samples are characterized by electron backscatter diffraction (EBSD).

III. RESULTS AND DISCUSSION

A. Shock-induced microstructure changes in polycrystalline NiTi

Detailed experimental conditions can refer to our previous work [26]. Two $Ni_{52}Ti_{48}$ samples with sizes of Φ8 mm × 0.877 mm are shocked by aluminum flyer plates with sizes of 26 mm × 12 mm × 1.002 mm at velocity 2.592 km s^{-1}, and the corresponding particle velocity U_p was 0.927 km s^{-1}. In experiments, one sample is monitored continuously with dual laser heterodyne velocimetry (DLHV) to obtain velocity profiles for calculating macroscopic material responses such as the elastic-plastic transition [Hugoniot elastic limits (HEL)] and pressure-volume states. The other sample is recovered after being shocked through copper momentum trapping and then analyzed using x-ray diffraction (XRD) and electron backscatter diffraction (EBSD) [Fig. 2(a)].

The results of XRD analysis show that there are only B2 NiTi austenite structure in both as-received and deformed samples, no phase transformation after shock loading [Fig. 3(g)]. And EBSD characterizations show lots of twins and new grains in the recovered sample corresponding to as-received sample [Figs. 3(a) and 3(b)]. Figures 3(c), and 3(d) are magnified region of the marked rectangular areas in Fig. 3(b), which represent twins and new grains, respectively. EBSD misorientation profiles of as-received and deformation samples show a misorientation angle of ∼70.5° occurrence [Figs. 3(e) and 3(f)], compared to {112} austenite twins. In summary, there is indeed no phase transformation in the shock loading experiments on B2 austenite near-equiatomic NiTi, and the plastic deformation modes at the high stain rates include dislocations, twins and new grains. In particular, {112} austenite twins in NEMD simulation are found in experiments, which is evident as specific peaks in the misorientation angle profiles.

To seek microscopic explanations for the shock response of polycrystalline NiTi alloys (Fig. 3), we carried out NEMD simulations of nc-NiTi under shock loading at ambient temperature 300 K and different shock loading velocities U_p, including 0.6 km s^{-1}, 0.8 km s^{-1}, and 1.0 km s^{-1} (Fig. 4). With the propagation of 35 ps-duration-pulse shock waves, there are diverse stress states in nc-NiTi [Fig. 4(a)]. Different stress states correspond to several stages are distinguished by red dashed lines in Figs. 4(b)–4(d), and they are marked as unshocked, shocked, unloading, and relaxed (completely released). No phase transformation occurs in our entire simulation [Fig. 4(e)], which is consistent with our experimental results [Fig. 3(g)]. And very similar plastic deformation characteristics of shocked NiTi samples are exhibited in macroscale experiments and microscale MD simulations.

Therefore plastic deformation, especially austenite twins and new grains are the focus of this study. To explain the underlying mechanism of twins and new grains, we must analyze their microstructural evolution. We also note that all twins generated in the simulations are of {112} type. For convenience, here we label twins at three different positions and stages in the our NEMD simulation of nc-NiTi as twin T1, T2, and T3. Meanwhile, NG represents new grain formed under shock loading.

B. Shock loading velocity dependence of deformation mode near the GBs triple junction

1. {112} *austenite twins nucleation and propagation at* $U_p = 0.6$ *km* s^{-1}

Plastic deformation such as slip and twinning are often thought to accompany the phase transformation of NiTi alloys, on the other hand, the phase transformation may take prece-

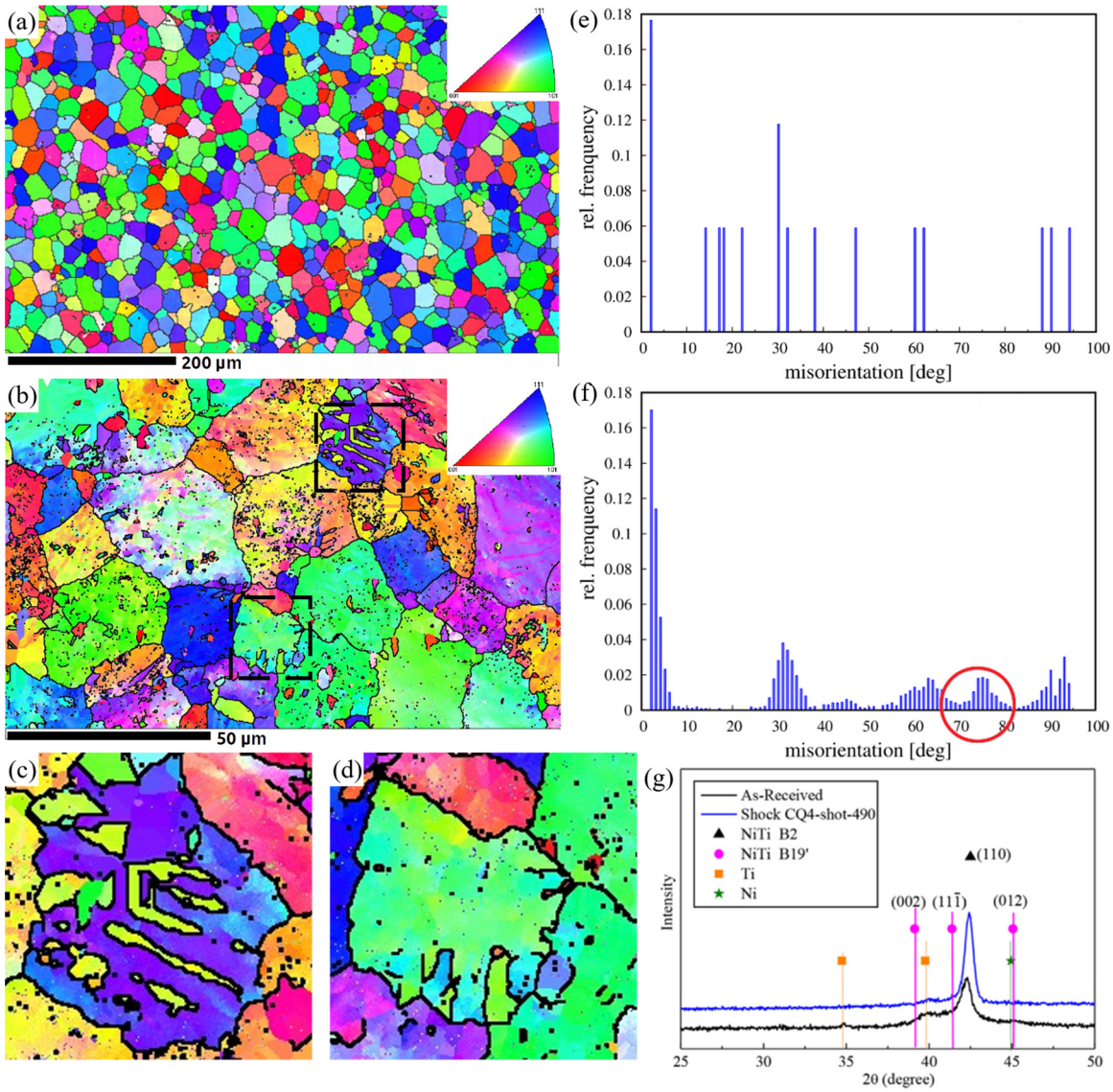

FIG. 3. (a)–(b) EBSD characterizations of as-received and experimentally recovered polycrystalline NiTi samples at shock loading velocity $U_p = 0.927$ km s^{-1} at room temperature. (c)–(d) The corresponding amplified configurations for the marked rectangular areas in (b), which represent twins and new grains, respectively. (e)–(f) The histograms of frequency and distribution of the boundaries for (a) and (b), respectively, the red circle corresponding to {112} austenite twins, 70.5° misorientation angle, and 5° for the maximum deviations. (g) The XRD analysis of as-received and experimentally recovered polycrystalline NiTi samples at shock loading velocity $U_p = 0.927$ km s^{-1} at room temperature.

dence over plastic deformation. That results in the complex deformation mechanism of NiTi alloys [54–57]. Theoretical calculations show that there are many slip systems in NiTi austenite: (011)[1$\bar{1}$1], (011)[0$\bar{1}$1], (011)[100], (001)⟨010⟩, and ($\bar{2}$11)[111], etc. Among them the (011)[100] slip system is most favorable and widespread with the minimum energy barrier of about 142 mJ m^{-2} via generalized stacking fault energy (GSFE) calculation [58]. The ($\bar{2}$11)[111] slip system is considered important because twinning mode can occur in this system. Its GSFE reaches the peak energy 847 mJ m^{-2} after gliding a displacement $\frac{a}{3}$[111] on ($\bar{2}$11) plane but for the $\frac{a}{3}$[$\bar{1}\bar{1}\bar{1}$] as 795 mJ m^{-2}, and for metastable superspatials $\frac{a}{2}$[111] as 692 mJ m^{-2}. They are higher than the energy required for activation of (011)[100] slip system [58], hence it is far less likely to occur. In this study, due to high loading strain rates and stresses, the activation of the ($\bar{2}$11)[111] slip system is, however, still possible.

In the literature on the B2 austenite, {112} and {114} twins have been reported [15]. While the formation of {112} twin in B2 austenite has always been controversial. Goo *et al.* proposed that by successively gliding a displacement of $\frac{a}{6}$[$\bar{1}\bar{1}\bar{1}$] on ($\bar{2}$11) plane, according to the formation mode of BCC metal twins, can form a new phase O structure in the shear region, the corresponding magnitude of the twinning shear $\gamma_{\frac{a}{6}[\bar{1}\bar{1}\bar{1}]}$ is 0.707 [59]. On the other hand, the perfect twin in B2 austenite can formed by successively gliding a displacement of $\frac{a}{3}$[111] on ($\bar{2}$11) plane, although it is often considered difficult to active for $\gamma_{\frac{a}{3}[111]} = 1.414$. For this

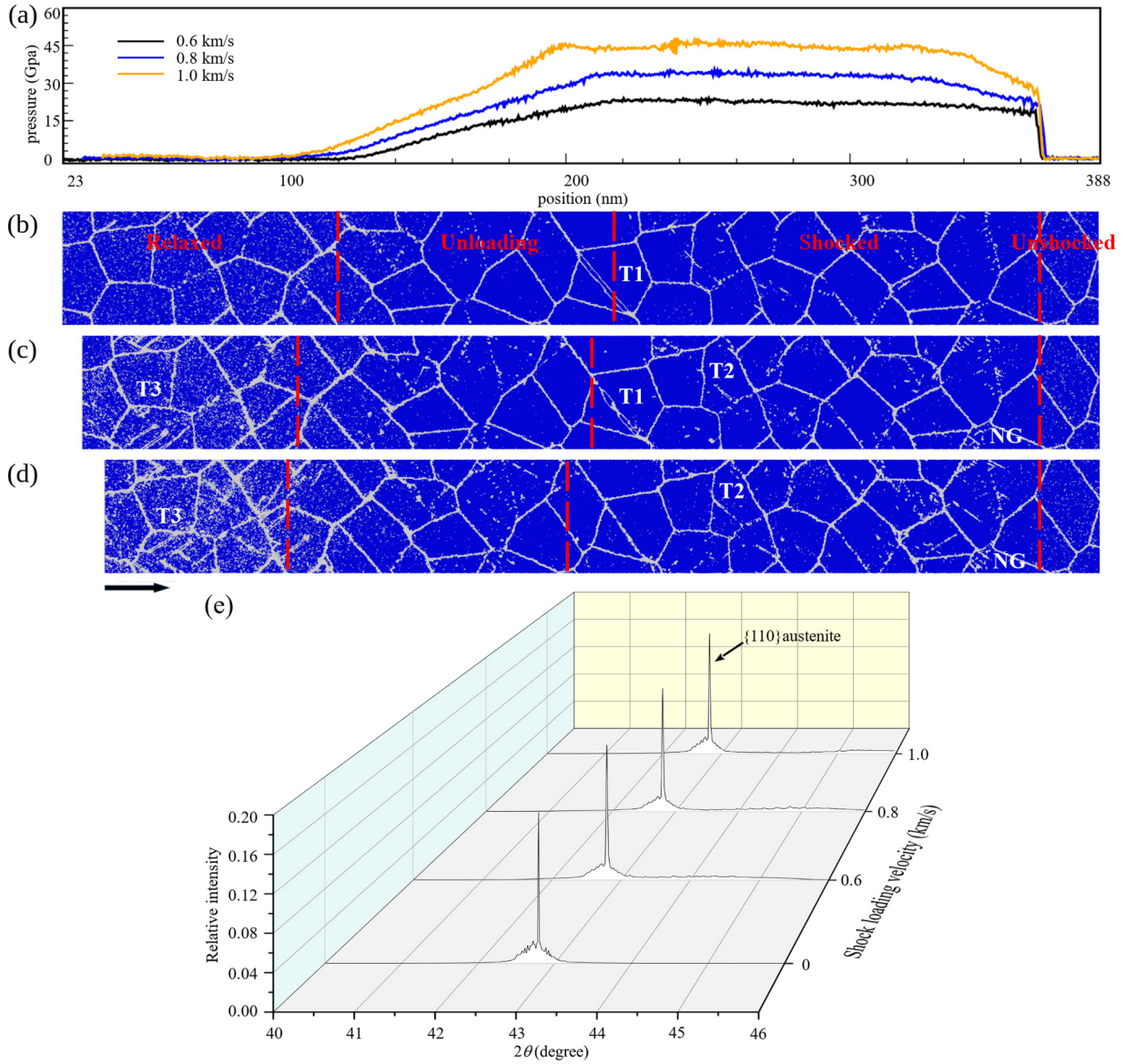

FIG. 4. The (a) 1D pressure profiles (σ_{xx}) in nc-NiTi under different shock-loading velocities U_p. Comparisons of simulated results corresponding to (a) at initial ambient temperature 300 K and different U_p: (b) 0.6 km s^{-1}; (c) 0.8 km s^{-1}; (d) 1.0 km s^{-1} (different states are distinguished by red long dashes). The microstructures are characterized by CNA methods: twin T1, T2, T3, and new grain (NG). The shock direction is labeled by black arrows. The simulated XRD patterns (e) of the nc-NiTi models for initial austenite [Fig. 2(b)], Fig. 4(b), 4(c) and 4(d), respectively.

reason, some researchers consider the formation of {112} twins is possible by combining shuffle among atoms on the basis of successively gliding a displacement of $\frac{a}{6}[\bar{1}\bar{1}\bar{1}]$ on $(\bar{2}11)$ plane, which provides a hypothesis for the formation of {112} twins [60]. Our NEMD simulations prove that {112} austenite twin in shock loading nc-NiTi can indeed be formed by successively gliding a displacement of $\frac{a}{3}[111]$ on $(\bar{2}11)$ plane.

Figure 5, represents the nucleation and propagation of deformation twin T1 under shock loading at $U_p = 0.6$ km s^{-1}. It can be seen from the atomic arrangement that the twin T1 belongs to {112} type. Under the compression of shock waves, twins nucleate from the GBs triple junction and the three layers twin embryo is formed at 39.0 ps. After the nucleation of twins, dislocations continue to glide on $(\bar{2}11)$ plane along the $\langle 111 \rangle$ until reaching a distance of $\frac{\sqrt{3}a}{3}$ (corresponding to $\frac{a}{3}[111]$ partial dislocations, $\gamma_{\frac{a}{3}[111]} = 1.414$). Then twin of three layers are formed completely in the sheared region without phase transformation (40.0 ps). Then another $\frac{a}{3}\langle 111 \rangle$ partial dislocation neighboring twins boundaries is activated, and a displacement of $\frac{\sqrt{3}a}{3}$ is glided, which leads to formation of five layers twin (41.5 ps). Finally, twin growth (thickening) is accomplished by repeating the process between 40.0–41.5 ps. That is, {112} austenite twin can be formed by successively gliding a displacement of $\frac{a}{3}[111]$ on $(\bar{2}11)$ plane. To better identify the twin T1 at 41.5 ps, CNA and OM analysis are used as shown in Fig. 5.

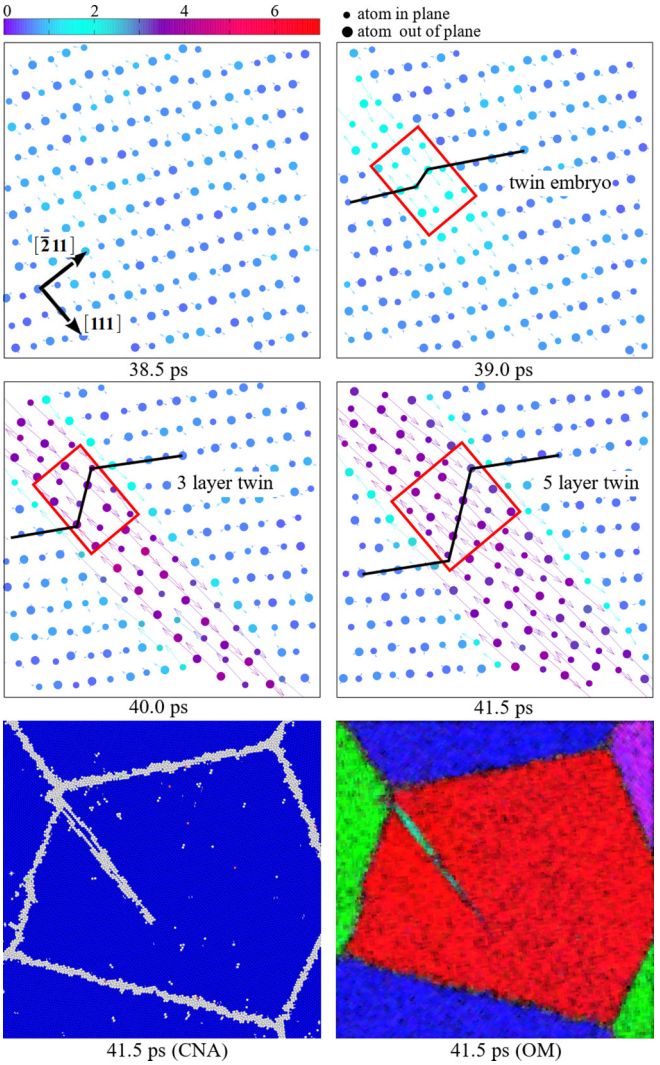

FIG. 5. Nucleation, propagation and growth of {112} twin T1 in austenite phase at shock loading velocities $U_p = 0.6$ km s^{-1} in nc-NiTi, which is formed by successively gliding a displacement of $\frac{a}{3}$[111] on ($\bar{2}$11) plane. The atom color coding is based on the MRD magnitude of $\boldsymbol{s}$, the cyan (corresponding to "4") represent dislocation $\frac{a}{3}$[111]. The arrows denote slip vectors and it is also colored by MRD magnitude of $\boldsymbol{s}$.

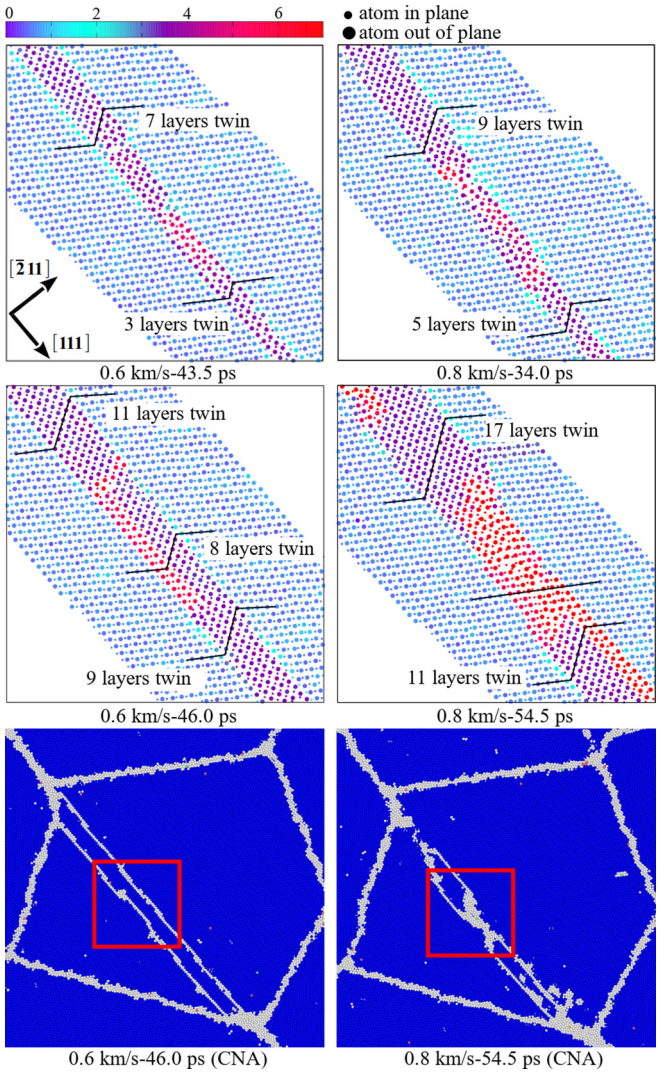

FIG. 6. Growth of {112} twin T1 in austenite at different shock loading velocities U_p in nc-NiTi. The first four pictures corresponds to amplified configurations for the marked rectangular areas in the last two. The atom color coding is based on the MRD magnitude of $\boldsymbol{s}$, the cyan and red (one each for 4 and 6) correspond to dislocations $\frac{a}{3}$[111] and $\frac{a}{2}$[111], respectively.

2. *Competition between twins and dislocations at $U_p = 0.6$ km s^{-1} and 0.8 km s^{-1}*

Twin T1 can be formed at $U_p = 0.6$ km s^{-1} and 0.8 km s^{-1} [Figs. 4(b) and 4(c)]. However, twin T1 is divided into two separate parts at $U_p = 0.8$ km s^{-1}. Detailed atomic deformations are shown in Fig. 6. For $U_p = 0.6$ km s^{-1}, twin T1 already propagated into the grain interiors at 43.5 ps. As introduced in the previous section, it is caused by $\frac{a}{3}$[111] partial dislocations. Note that there is a total displacement of $\frac{\sqrt{3}}{2}$a ($\frac{a}{3}$[111] + $\frac{a}{6}$[111] → $\frac{a}{2}$[111], $\gamma_{\frac{a}{2}[111]} = 2.121$) on the ($\bar{2}$11) plane along ⟨111⟩ direction (the red part, number 6) under continuous shock loading until 70.0 ps [58]. Although B2 struture is distinct from BCC for its full dislocation on {112} plane is a⟨111⟩ instead of $\frac{a}{2}$⟨111⟩, $\frac{a}{2}$⟨111⟩ in this study also leads to partial detwinning at 46.0 ps like BCC metal Ta [48,61]. Nevertheless, that leads to the local incompatibility and hinders the $\frac{a}{3}$[111] dislocation emission, this means that it can inhibit the thickening of twin T1 in this region. For $U_p = 0.8$ km s^{-1}, the displacement of $\frac{\sqrt{3}}{2}$a on the ($\bar{2}$11) plane along ⟨111⟩ direction (the red part, number 6) causes the fully detwinning in the corresponding area (54.5 ps).

3. *Amorphous shear band at $U_p = 1.0$ km s^{-1}*

Different from the situations at $U_p = 0.6$ km s^{-1} and 0.8 km s^{-1}, amorphous shear band is generated from the GBs triple junction, instead of twins [Fig. 4(d)]. Its formation process is illustrated in Fig. 7. When the shock wave passes through the GBs triple junction, there is accumulation of local stresses in this region (27.5 ps). Once the resolved shear stress on the GB $\tau_{\rm rss}$ exceeds the corresponding critical resolved shear stress $\tau_{\rm crss}$, GB sliding occurs (35.0 ps). In essence, the

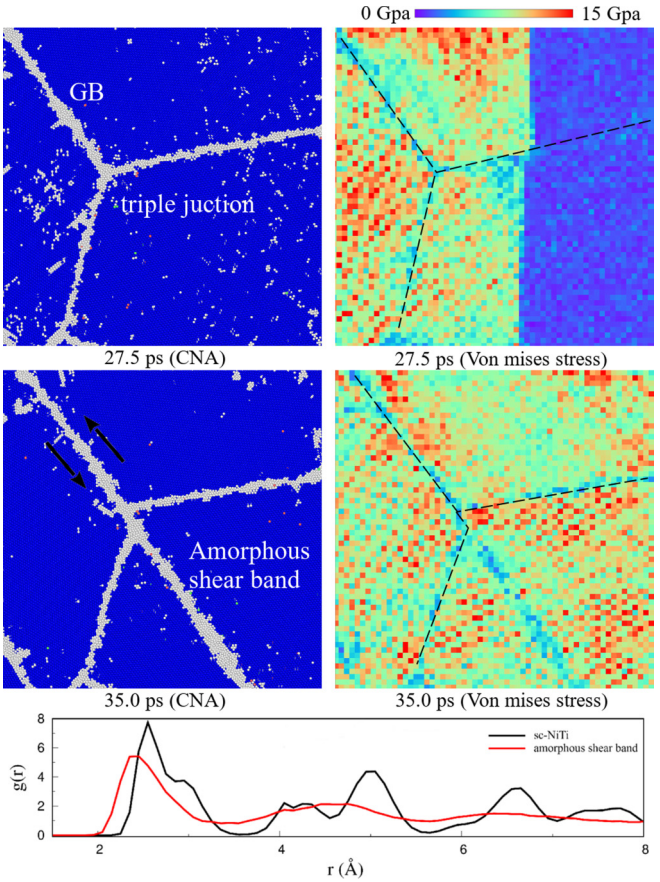

FIG. 7. Formation of amorphous shear band at grain boundaries (GBs) triple junction at shock loading velocity $U_p = 1.0$ km s^{-1}, characterization by CNA analysis and distribution of von Mises shear stress τ^{Mises} in the same region. We also calculate radical distribution function [$g(r)$] of the B2 structure sc-NiTi and amorphous shear band in nc-NiTi.

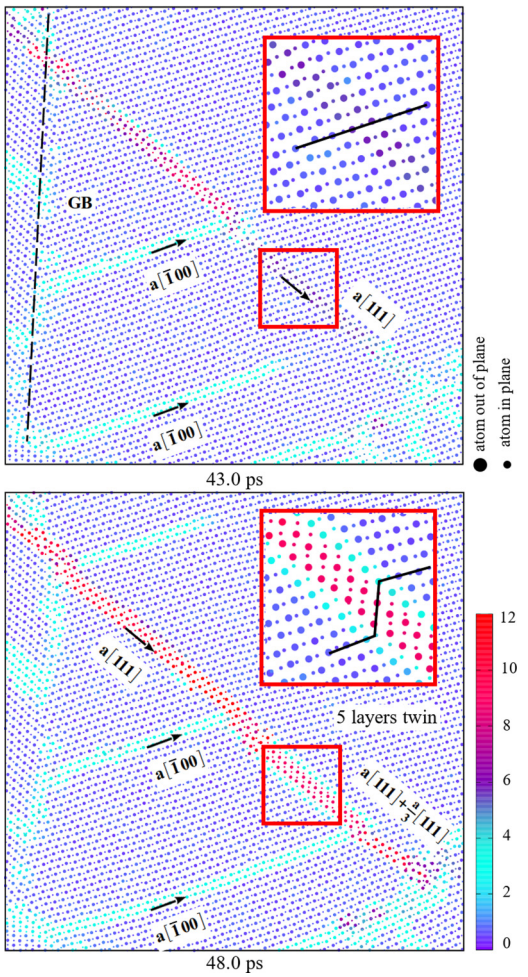

FIG. 8. Details of twin T2 at shock loading velocity $U_p = 0.8$ km s^{-1}. The atom color coding is based on the MRD magnitude of $\boldsymbol{s}$.

advanced twinning modes at $U_p = 0.6$ km s^{-1} and 0.8 km s^{-1} (Figs. 5 and 6), contribute to additional strain accommodation when slip systems are unavailable.

When the local stress continues to increase and finally exceeds the strain accommodation capability of the twin (and dislocation) mode, and it leads to the nucleation of amorphous shear band from the GBs triple junctions (35.0 ps) [62]. To identify that amorphous in the region mentioned above, we calculate radial distribution function (RDF) of the B2 structure sc-NiTi and amorphous shear band in nc-NiTi at $U_p = 1.0$ km s^{-1} (Fig. 6).

C. Other twins formed in the different loading stages and locations in MD

Like twin T1 at $U_p = 0.6$ km s^{-1} and 0.8 km s^{-1}, twin T2 is also formed during the shock loading process, but it is not generated from the GBs triple junction. The evolution is detailed in Fig. 8. Dislocations inside the left grain propagate to the GB, and then they are absorbed by GB. Then GB plays roles as the nucleation site of new dislocations, and newly formed dislocations propagate into the right grain with other slip systems [63,64]. New dislocations with $\{112\}\langle111\rangle$ and $\{110\}\langle100\rangle$ slip systems are emitted at $U_p = 0.8$ km s^{-1} (43.0 ps), and more dislocations are generated at higher velocity. At 48.0 ps, dislocations with $\{112\}\langle111\rangle$ slip system can interact with two parallel dislocations of same $\{110\}\langle100\rangle$ slip system, which then results in twin formation. Twin T2 also can be formed at a higher shock loading velocity $U_p = 1.0$ km s^{-1}, but not at $U_p = 0.6$ km s^{-1}.

In our NEMD simulations, twins are not only formed during shock compression, e.g., twin T1 and T2, but also in the unloading process, e.g., twin T3 (Fig. 4). Twin T3 evolution at $U_p = 0.8$ km s^{-1} is detailed in Fig. 9. At 34.5 ps, there are slip bands in the grain due to plastic deformation with $\{112\}\langle111\rangle$ slip system before start of unloading. New dislocations emitted from the interaction of slip bands during release process, and eventually evolve into stable twin (47.5 ps) [65]. Shock loading velocity U_p has an important influence on the generation of twin T3, which is specifically manifested in that more slip bands generated at higher U_p are more conducive to twin formation. After the unloading waves have completely traveled through the region, there are still twins in the region at $U_p = 0.8$ km s^{-1} and 1.0 km s^{-1}. But twin will not be generated at $U_p = 0.6$ km s^{-1}.

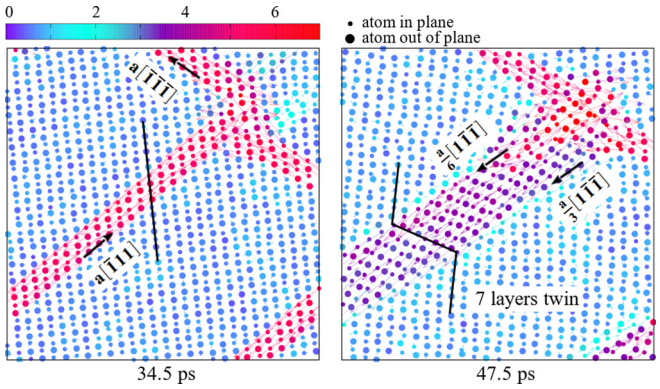

FIG. 9. Details of twin T3 at shock loading velocity $U_p = 0.8$ km s^{-1}. The atom color coding is based on the MRD magnitude of $\boldsymbol{s}$.

D. Nanoscale rotational deformation leads to new grain in nc-NiTi

Typically, new grains (NGs) under high strain rates shock loading are interpreted as undergoing several stages: amorphous, recrystallization, and grain refinement, caused by homogeneous activation of slip system and their interaction inside the grain [66,67]. Our NEMD simulations indicate that there may be another formation mode of NGs in nc-NiTi: NGs can be formed by the nanoscale rotational deformation (NRD) at high stresses [68–70].

As shown in Fig. 1(a), the parental grain (PG) is composed of a large angle grain boundary (LAGB) and a small angle grain boundary (SAGB). At $U_p = 0.8$ km s^{-1}, after the shock wave passes through this area, the collective events of nanoscale ideal shear occur at both LAGB and SAGB. This results in several dislocations with the same $\{112\}\langle 111\rangle$ slip system excited from the LAGB (and SAGB with $\{110\}\langle 100\rangle$ slip system), and the distance between the adjacent dislocation slip planes is only about two lattice widths [Fig. 10(b)].

A wall of nanodisturbance is generated in the dislocation glide region [Fig. 10(b)], which consists of a dipole of noncrystallographic dislocations with tiny Burgers vector $\pm\boldsymbol{b}$ (smaller than the corresponding perfect dislocations, e.g., a$\langle 111\rangle$, a$\langle 100\rangle$). The parallel wall of nanodisturbance will

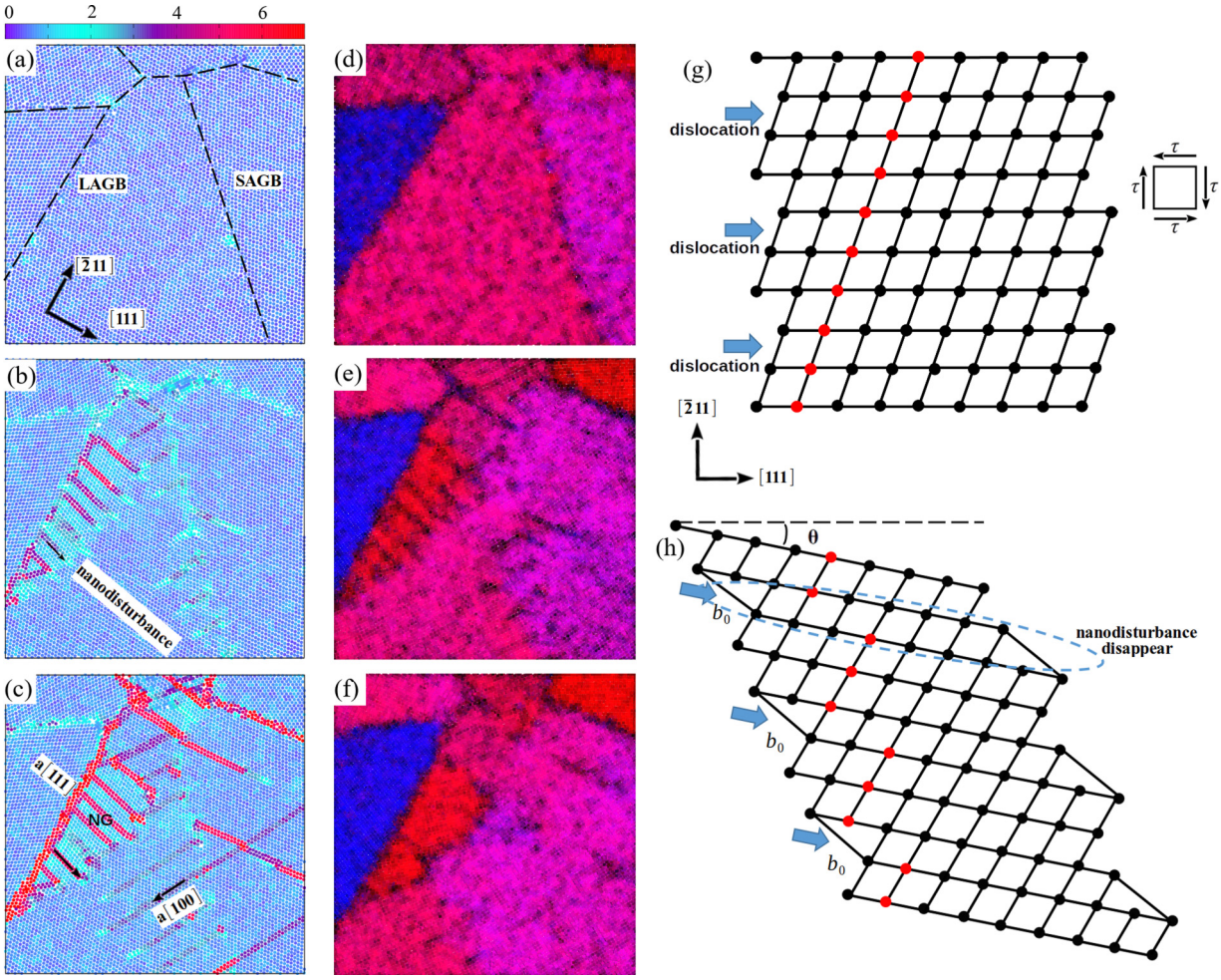

FIG. 10. (a)–(c) The microstructural evolution of new grain NG for shock loading velocity $U_p = 0.8$ km s^{-1} at 15.0 ps, 21.5 ps and 46.0 ps, respectively. The atom color coding is based on the MRD magnitude of $\boldsymbol{s}$. (d)–(f) The corresponding region based on OM analysis along the x axis. (g)–(h) Projection of B2 crystal position on $(0\bar{1}1)$ plane before (g) and after (h) deformation.

cause the rotation deformation in this region. As the magnitude of $\boldsymbol{b}$ increases to perfect dislocation $\boldsymbol{b_0}$, the wall of nanodisturbance finally disappears, and the entire region corresponding to the parallel dislocations eventually completes the rotation. Considering that both the LAGB and SAGB of PG emit dislocations towards the interior of grain at $U_p = 0.8$ km s^{-1}, the slip systems of dislocations emitted from LAGB and SAGB are different, these dislocations meet and interact in the PG interior. Then dislocation propagation is hindered and GBs are generated in the dislocation interaction region, that is, new grains are formed [69] [Fig. 10(c)]. The formation process of new grain NG can be more clearly identified by OM method, the orientation of NG is clearly different from the PG. Schematic diagram of the NRD by ⟨111⟩ dislocation in NiTi is also illustrated in Figs. 10(g)–10(h).

The increase of shock loading velocity U_p is conducive to the generation of dislocations with the same slip system at the GBs, and then the new grains caused by NRD are produced (0.8 km s^{-1} and 1.0 km s^{-1}). At $U_p = 0.6$ km s^{-1}, there are only collective events of dislocations generated from the LAGB, therefore, no dislocation interaction occurs and no new grains will be produced.

In our dynamic shock loading experiments of NiTi on pulsed power generator CQ-4, NGs are found in EBSD analysis of samples recovered from the shock loading experiments at $U_p = 0.927$ km s^{-1} [Fig. 3(d)]. The corresponding pressure is 34.4 Gpa and the strain rate is about 10^6 s^{-1}. In doing so, materials may need NRD to provide high plastic strain rates other than conventional dislocations generation mechanisms. So it makes sense for the NRD leading to NGs when the collective neighboring wall of nanodisturbances with different shear direction are generated [69].

IV. CONCLUSION

We conduct NEMD simulations to study the shock-induced {112} austenite twins and NGs in columnar nc-NiTi. The shock loading experiments based on pulsed power generator CQ-4 provide evidence of {112} deformation twins and NGs. The results of NEMD simulation present very similar characteristics of microstructure with the EBSD results of shock recovered NiTi samples. The main conclusions are listed below:

(i) No twins occur in the sc-NiTi under shock loading, while GBs triple junction and the slip bands interaction of different slip systems in nc-NiTi serve as nucleations for {112} austenite twins.

(ii) Shock-induced {112} twins in austenite in our NEMD simulations can be formed by successively gliding a displacement of $\frac{a}{3}[111]$ on $(\bar{2}11)$ plane.

(iii) New grains NGs in our NEMD simulations are formed by nanoscale rotational deformation (NRD) under shock loading at extreme high strain rates.

(iv) The shock loading velocity U_p related shear stress τ plays key role in twins and NGs. As the U_p increases, amorphous shear bands instead of twins T1 are generated from GBs triple junction. On the other hand, the increase of U_p leads to more types and quantities of slip bands, which provides more possibilities for twins T2 and T3 generated at the intersection of slip bands. Similarly, higher U_p is beneficial to the collective events of ideal nanoscale rotational deformation on the both sides (LAGB and SAGB) of parental grain PG.

Some limitations exist in our work, such as its relatively small sizes and limited number of configurations. Despite this we believe our work could be a springboard for understanding the microstructure deformation mechanism of NiTi alloy at high strain rates, which helps to build physics-based strength models.

Due to the limitation of potential accuracy, MD simulations can only reproduce the experimental phenomena in the limited pressure range. Moreover, given the small simulation sample size, caution must be exercised. Future studies can focus on improving the potential function and further increasing the scale of the simulation system, which could be used to simulate the properties of NiTi under higher pressure and more complex extreme conditions, including considering the effects of initial defects and radiation simulation, etc.

ACKNOWLEDGMENTS

This work was partially supported by the project of the National Natural Science Foundation of China (Grant No. 11972031). We are grateful to the Advanced Analysis and Computation Center of CUMT for the award of CPU hours to accomplish this work. The authors wish to thank Prof. T. Zhu at Georgia Institute of Technology for providing the improved potential of NiTi. We also thank The Peac Institute of Multiscale Sciences (PIMS) for the use of OM analysis tool.

[1] N. Morgan, Mater. Sci. Eng. A **378**, 16 (2004).
[2] D. Stoeckel, Mater. Des. **11**, 302 (1990).
[3] C. Bil, K. Massey, and E. J. Abdullah, J. Intell. Mater. Syst. Struct. **24**, 879 (2013).
[4] Y. Furuya, J. Intell. Mater. Syst. Struct. **7**, 321 (1996).
[5] E. Chau, C. Friend, D. Allen, J. Hora, and J. Webster, Mater. Sci. Eng. A **438–440**, 589 (2006).
[6] L. Lecce and A. Concilio, *Shape Memory Alloy Engineering: For Aerospace, Structural and Biomedical Applications* (Oxford University Press, Oxford, 2003).
[7] J. N. R. Ashwin Rao and A. R. Srinivasa, *Design of Shape Memory Alloy (SMA) Actuators* (Springer, Berlin, 2015).
[8] W. W. Chen, Q. Wu, J. H. Kang, and N. A. Winfree, Int. J. Solids Struct. **38**, 8989 (2001).
[9] S. Nemat-Nasser, J.-Y. Choi, W.-G. Guo, and J. B. Isaacs, Mech. Mater. **37**, 287 (2005).
[10] N.-N. S, Y. C. J, G. W, I. JB, and T. M, Trans. ASME, J. Eng. Mater. Technol. **127**, 83 (2005).
[11] W. Guo, J. Su, Y. Su, and S. Chu, J. Alloys Compd. **501**, 70 (2010).

[12] Y. Qiu, M. L. Young, and X. Nie, Shape Memory Superelasticity **1**, 310 (2015).
[13] A. M. Thakur, N. N. Thadhani, and R. B. Schwarz, Metall. Mater. Trans. A **28**, 1445 (1997).
[14] S. V. Razorenov, G. V. Garkushin, O. A. Kanel', G. I. Kashin, and I. V. Ratochka, Phys. Solid State **53**, 824 (2011).
[15] P. Chowdhury and H. Sehitoglu, Prog. Mater. Sci. **88**, 49 (2017).
[16] Y. Zhong, K. Gall, and T. Zhu, J. Appl. Phys. **110**, 033532 (2011).
[17] Q. Yin, X. Wu, and C. Huang, Philos. Mag. **97**, 1311 (2017).
[18] F. Yazdandoost and R. Mirzaeifar, Shape Memory Superelasticity **4**, 435 (2018).
[19] W.-S. Ko, B. Grabowski, and J. Neugebauer, Phys. Rev. B **92**, 134107 (2015).
[20] M. Wang, S. Jiang, and Y. Zhang, Materials (Basel, Switzerland) **11**, 2334 (2018).
[21] J. C. F. Millett, N. K. Bourne, and G. T. Gray, J. Appl. Phys. **92**, 3107 (2002).
[22] J. Millett and N. Bourne, Mater. Sci. Eng.: A **378**, 138 (2004).
[23] Y. J. E. Meziere, J. C. F. Millett, N. K. Bourne, A. Wallwork, and A. Workman, in *Shock Compression of Condensed Matter - 2005: Proceedings of the Conference of the American Physical Society Topical Group on Shock Compression of Condensed Matter*, edited by M. D. Furnish, M. Elert, T. P. Russell, and C. T. White, AIP Conf. Proc. 845 (AIP, New York, 2006), p. 749.
[24] Y. J. E. Meziere, J. C. F. Millett, and N. K. Bourne, J. Appl. Phys. **100**, 033513 (2006).
[25] R. Hackenberg, D. Swift, J. Cooley, K. C. Chen, D. Thoma, D. Paisley, and A. Hauer, in *International Workshop on New Models and Hydrocodes for Shock Wave Processes in Condensed Matter* (Russian Academy of Science, Moscow, 2002).
[26] X. Zhang, G. Wang, B. Luo, S. N. Bland, F. Tan, F. Zhao, J. Zhao, C. Sun, and C. Liu, J. Alloys Compd. **731**, 569 (2018).
[27] S. J. Tracy, S. J. Turneaure, and T. S. Duffy, Phys. Rev. Lett. **120**, 135702 (2018).
[28] S. Plimpton, J. Comput. Phys. **117**, 1 (1995).
[29] W. S. Lai and B. X. Liu, J. Phys.: Condens. Matter **12**, L53 (2000).
[30] H. Zong, T. Lookman, X. Ding, S.-N. Luo, and J. Sun, Acta Mater. **65**, 10 (2014).
[31] Y. Cai, F. P. Zhao, Q. An, H. A. Wu, W. A. Goddard, and S. N. Luo, J. Chem. Phys. **139**, 164704 (2013).
[32] F. Shimizu, S. Ogata, and J. Li, Mater. Trans. **48**, 2923 (2007).
[33] A. Okabe, B. Boots, and K. Sugihara, *Wiley Series in Probability and Mathematical Statistics* (Wiley, New York, 1992).
[34] S. Nosé, J. Chem. Phys. **81**, 511 (1984).
[35] W. G. Hoover, Phys. Rev. A **31**, 1695 (1985).
[36] B. L. Holian, Shock Waves **5**, 149 (1995).
[37] H. Jarmakani, E. Bringa, P. Erhart, B. Remington, Y. Wang, N. Vo, and M. Meyers, Acta Mater. **56**, 5584 (2008).
[38] H. Tsuzuki, P. S. Branicio, and J. P. Rino, Comput. Phys. Commun. **177**, 518 (2007).
[39] A. Stukowski, Modell. Simul. Mater. Sci. Eng. **18**, 015012 (2010).
[40] W.-S. Ko, S. B. Maisel, B. Grabowski, J. B. Jeon, and J. Neugebauer, Acta Mater. **123**, 90 (2017).
[41] M. L. Falk and J. S. Langer, Phys. Rev. E **57**, 7192 (1998).
[42] L. C. S. P. Coleman and D. E. Spearot, Modell. Simul. Mater. Sci. Eng. **21**, 055020 (2013).
[43] T. E. Faber and J. M. Ziman, Philos. Mag. **11**, 153 (1965).
[44] L. Wang, J. C. E, Y. Cai, F. Zhao, D. Fan, and S. N. Luo, J. Appl. Phys. **117**, 084301 (2015).
[45] J. E, M. Tang, D. Fan, L. Wang, and S. Luo, Comput. Mater. Sci. **153**, 338 (2018).
[46] J. A. Zimmerman, C. L. Kelchner, P. A. Klein, J. C. Hamilton, and S. M. Foiles, Phys. Rev. Lett. **87**, 165507 (2001).
[47] B. Arman, C. Brandl, S. N. Luo, T. C. Germann, A. Misra, and T. Çağin, J. Appl. Phys. **110**, 043539 (2011).
[48] L. Wang, F. Zhao, F. P. Zhao, Y. Cai, Q. An, and S. Luo, J. Appl. Phys. **115**, 053528 (2014).
[49] S.-N. Luo, Q. An, T. C. Germann, and L.-B. Han, J. Appl. Phys. **106**, 013502 (2009).
[50] S.-N. Luo, T. C. Germann, T. G. Desai, D. L. Tonks, and Q. An, J. Appl. Phys. **107**, 123507 (2010).
[51] G. Wang, B. Luo, X. Zhang, J. Zhao, C. Sun, F. Tan, T. Chong, J. Mo, G. Wu, and Y. Tao, Rev. Sci. Instrum. **84**, 015117 (2013).
[52] X. Zhang, G. Wang, J. Zhao, F. Tan, B. Luo, and C. Sun, Rev. Sci. Instrum. **85**, 055110 (2014).
[53] R. N. Orava and R. H. Wittman, in *Proceedings of the fifth International Conference on High Energy Rate Fabrication* (University of Denver, Denver, 1975).
[54] D. Norfleet, P. Sarosi, S. Manchiraju, M.-X. Wagner, M. Uchic, P. Anderson, and M. Mills, Acta Mater. **57**, 3549 (2009).
[55] Y. Liu, Z. Xie, J. V. Humbeeck, and L. Delaey, Acta Mater. **46**, 4325 (1998).
[56] P. Chowdhury and H. Sehitoglu, Prog. Mater. Sci. **85**, 1 (2017).
[57] I. Karaman, A. V. Kulkarni, and Z. P. Luo, Philos. Mag. **85**, 1729 (2005).
[58] T. Ezaz, J. Wang, H. Sehitoglu, and H. Maier, Acta Mater. **61**, 67 (2013).
[59] E. Goo, T. Duerig, K. Melton, and R. Sinclair, Acta Metall. **33**, 1725 (1985).
[60] T. Ezaz and H. Sehitoglu, Appl. Phys. Lett. **98**, 241906 (2011).
[61] S. Li, X. Ding, J. Deng, T. Lookman, J. Li, X. Ren, J. Sun, and A. Saxena, Phys. Rev. B **82**, 205435 (2010).
[62] H. Luo, H. Sheng, H. Zhang, F. Wang, J. Fan, J. Du, J. Ping Liu, and I. Szlufarska, Nature Commun. **10**, 3587 (2019).
[63] I. Beyerlein, M. Demkowicz, A. Misra, and B. Uberuaga, Prog. Mater. Sci. **74**, 125 (2015).
[64] C. Lv, J. Yang, X. Zhang, Y. Cai, X. Liu, G. Wang, and S.-N. Luo, J. Phys. D: Appl. Phys. **51**, 335301 (2018).
[65] J. Christian and S. Mahajan, Prog. Mater. Sci. **39**, 1 (1995).
[66] M. X. Tang, J. C. E, L. Wang, and S. N. Luo, J. Appl. Phys. **121**, 115901 (2017).
[67] L. Wang, B. Li, X. L. Deng, W. R. Jian, M. Shang, L. Deng, X. M. Zhang, J. F. Tang, and W. Y. Hu, Phys. Rev. B **99**, 174103 (2019).
[68] S. V. Bobylev, N. F. Morozov, and I. A. Ovid'ko, Phys. Rev. Lett. **105**, 055504 (2010).
[69] I. A. Ovid'ko and A. G. Sheinerman, Appl. Phys. Lett. **98**, 181909 (2011).
[70] S. V. Bobylev, N. F. Morozov, and I. A. Ovid'ko, Phys. Rev. B **84**, 094103 (2011).